Catal Lett (2008) 121:179–188
DOI 10.1007/s10562-007-9364-6

Effect of Co Content Upon the Bulk Structure of Sr- and Co-doped $LaFeO_3$

John N. Kuhn · Umit S. Ozkan

Received: 14 September 2007 / Accepted: 26 November 2007 / Published online: 12 December 2007

Abstract The bulk structure was investigated for Fe-based perovskite-type oxides with the formula $La_{0.6}Sr_{0.4}Co_yFe_{1-y}O_{3-\delta}$ (y = 0.1, 0.2, and 0.3). The materials were confirmed to be stoichiometric with respect to oxygen under ambient conditions and the structural features were then further characterized under different environments as a function of temperature. Under reducing atmospheres, the degree of reduction increased with Co content, suggesting the presence of preferential oxidation of Fe over Co. Under milder conditions, oxygen vacancy formation was not proportional to Co content, which was likely caused by an electronic structure transition. The unit cell parameters were also shown to strongly depend upon Co content, temperature, and environment. A rhombohedral to cubic transition occurred at lower temperatures for higher Co content, but showed less dependence upon environment. A change in the thermal expansion behavior occurred at the temperature where oxygen vacancies formed leading to two regions of linear thermal expansion. The use of lattice parameters compared to dilatometry allowed for the simultaneous monitoring of unit cell symmetry and expansion behavior so the link between thermal properties and unit cell symmetry could be firmly established.

Keywords Perovskite-type oxides · High temperature phase transition · In-situ XRD · Oxygen nonstoichiometry

J. N. Kuhn · U. S. Ozkan (✉)
Department of Chemical and Biomolecular Engineering, The Ohio State University, Columbus, OH 43210, USA
e-mail: Ozkan.1@osu.edu

1 Introduction

Fe and Co-based perovskite-type (ABO_3) oxides are mixed conductors due to their simultaneous ability to conduct electrons and oxide ions. Due to this interesting ability, perovskite-type oxides are important for a number of technologies including oxygen sensors, oxygen separation and liberation devices, solid oxide fuel cell (SOFC) electrodes, and heterogeneous catalysis. In particular, the application of these materials is of great interest for SOFCs since other cathode material options are limited to precious metal—ceramic materials. Recent research regarding the use of Co-based mixed conductors as SOFC cathodes demonstrated that bulk ionic transport and the surface exchange kinetics of the oxygen reduction reaction (ORR) co-limit SOFC performance [1]. Since these properties depend upon the bulk structure, a thorough structural understanding is needed. Solid solutions of Co and Fe in the Fe-rich formulations are of great interest due to their increased relevance toward SOFCs using zirconia-based electrolytes. For SOFC applications, an understanding of the high temperature thermal behavior is necessary to eliminate or at least to minimize effects caused by expansion differences at the electrode–electrolyte interface.

Oxygen ion mobility occurs by the random hopping of oxygen vacancies in the anion framework of the oxide materials. Oxygen vacancies are formed by creating charge imbalances in the material. In perovskite-type oxides, it generally occurs by doping the normally trivalent A-site (La) with divalent cations (Sr). Additionally, the amount of oxygen vacancies increase as temperature increases, the reducing nature of the environment (typically expressed as the oxygen partial pressure) increases, and through the selection of reducible B-site cations. Oxygen vacancy formation in Co, Fe, and Mn perovskite-type oxides was

studied and the ease of forming oxygen vacancies was found to increase in the following order: Mn < Fe < Co [2–4]. To take advantage of the stability of Fe and conductivity of Co, oxygen vacancy formation in solid solutions of Co and Fe were also studied [5–8]. However, none of these studies examined variations in Fe-rich formulations with the most common A-site dopant level, 40% Sr ($La_{0.6}Sr_{0.4}Co_yFe_{1-y}O_{3-\delta}$ when y < 0.4).

While the ideal perovskite structure is a cubic phase with the Pm3m-O_h space group, perovskite-type oxides are capable of showing deviations from the ideal structure as they distort to orthorhombic, rhombohedral, tetragonal, monoclinic, and triclinic phases [9]. Fe-based perovskite-type oxides are orthorhombic, rhombohedral, or cubic depending upon the occupancy of the A- and B-sites at room temperature [6, 7]. These studies also inferred, from nonlinear dilatometry results, high temperature transitions to higher unit cell symmetry in oxygen-rich environments. No studies directly measured the unit cell symmetry as a function of temperature and environment for Fe-rich formulations. Wang and his coworkers showed that, for $La_{0.6}Sr_{0.4}Co_{0.8}Fe_{0.2}O_{3-\delta}$, the rhombohedral to cubic transition in air occurred near 450 °C, a slightly higher temperature than for pure Co-materials [10, 11]. Thus, the transition for Fe-rich formulations would be expected to occur above 450 °C. The level of symmetry in perovskite-type structures has a remarkable influence on performance.

A more symmetric unit cell allows for a more equivalent potential between occupied and vacant sites. The best known example of structure–property relationship involves reduced oxygen permeability when the perovskite unit cell symmetry undergoes the transition from cubic to orthorhombic (Brownmillerite-type phase) [12–17]. For cubic symmetry, the B-site is octahedrally coordinated by oxygen and oxygen vacancies occur randomly. On the other hand, orthorhombic symmetry contains both octahedrally and tetrahedrally coordinated B-sites and oxygen vacancies are no longer random. The effect of the rhombohedral to cubic transition upon the properties has not been examined.

The present work examines the bulk structure of $La_{0.6}Sr_{0.4}Co_yFe_{1-y}O_{3-\delta}$ for y = 0.1, 0.2, and 0.3. The evolution of the perovskite phase during the solid state reaction was examined in-situ. A rhombohedral to cubic phase transition is investigated as a function of Co content, temperature and atmosphere using in-situ XRD. Oxygen vacancy formation is determined using temperature-programmed techniques. Changes in thermal expansion coefficients (TECs) are monitored with respect to Co content, temperature and atmosphere. Some of the discrepancies reported in the literature for similar systems are also addressed.

2 Experimental

2.1 Sample Preparation

Metal carbonate and oxide precursors (minimum purity 99.7%) were Co_3O_4 (Aldrich), La_2O_3 (Fisher), Fe_2O_3 (J.T. Baker), and $SrCO_3$ (Alfa Aesar). Stoichiometric proportions of precursors (10 g total) were added to a half-pint ceramic milling jar (U.S. Stoneware) with 1.6–2.5 mm diameter zirconia grinding beads (20 g) and distilled water. The mixture was milled for 24 h at 120 RPMs using a long roll jar mill (U.S. Stoneware). After milling, the grinding beads were removed by sieving and mixtures were dried at ~75 °C. The dried material was crushed and then reacted at 1,000 °C (heating and cooling rate = 5 °C/min) for 48 h (Lindberg Blue tube furnace) in air to arrive at the perovskite structure. The resultant material was again crushed for uniform particle size (between 100 and 150 mesh) distribution. Surface area measurements were made by the physical adsorption of Kr at 77 K on a Micromeritics ASAP 2010.

2.2 X-ray Diffraction (XRD)

X-ray diffraction patterns were recorded with a Bruker D8 Advance diffractometer equipped with an HTK 1200 sample holder capable of controlling temperature and atmosphere. The instrument was outfitted with a Cu $K_{\alpha 1}$ radiation source, an incident beam Ge (111) monochromator, incident beam Soller slits, and a Braun position sensitive detector (PSD). The current and the voltage were 50 mA and 40 kV, respectively. Room temperature measurements were made using a 9-sample holder (polyethylene holders with a 0.5 mm deep reservoir) while rotating and were acquired for $2-\theta$ values from 20 to 90° at a step size of 0.0144° and a dwell time of 1 s.

In-situ measurements were made with the HTK 1200 oven implemented with graphite windows. Acquisition parameters were the same as above except no rotation was used and the step size was 0.0360°. Samples were supported on an alumina holder with a 0.5 mm deep reservoir. Heating and cooling rates of 10 °C/min and a 20 min hold time (5 min for solid-state reaction) before data acquisition at each temperature were also employed. The flow rate of the gas, 5% H_2/N_2, N_2, or air, was 10 mL/min. X-ray line profile analysis (Xfit) software package was used for peak fitting the data. Unit cell parameters were determined using a least-squares fit.

2.3 Temperature-programmed Reduction (TPR)

Temperature-programmed reduction studies were conducted with an in-house built system equipped with a thermal conductivity detector (TCD) and flow control capabilities. Samples ($\sim$85 mg) were loaded into a quartz U-tube reactor with plugs of silica wool. Samples were pretreated in 20 mL/min of 10% O_2/He at 550°C (10°C/min) with an isothermal hold time of 20 min in order to clean the surface of any adsorbed species. Samples were cooled under the same flow at 5 °C/min. Reduction data were collected via a TCD while flowing 30 mL/min of 10% H_2/N_2 as the temperature linearly ramped from room temperature to 900 °C. A water trap existed between the reactor and the TCD to ensure accurate H_2 consumption measurements. For each sample, the experiment was performed at 3 ramp rates (3.3, 5.5, and 10.0 °C/min). The temperature was held at 900 °C to get the TCD signal back to the baseline. Quantitative analysis of oxygen content was determined by calibrating the H_2 consumption necessary to completely reduce CuO and AgO. The calibration was repeated several times within 3% relative difference and accurately predicted the complete reduction of Co_3O_4. Data reduction was performed with the Grams AI software package.

2.4 Thermogravimetric Analyses (TGA)

The in-situ solid-state reaction was performed in a Perkin–Elmer TGA7. Samples were loaded into the Pt sample cup. Air at 50 mL/min was sent to the instrument. The temperature was ramped from room temperature to 1,100 °C at 5 °C/min.

Oxygen vacancy formation in air was monitored using Setaram TG-DSC111, an instrument with simultaneous thermogravimetry and scanning calorimetry abilities. The instrument was flow balanced and blank corrections were performed. Samples ($\sim$85 mg) were loaded into Pt sample cups. A steady mass was obtained at room temperature before starting 15 mL/min flow of air. The sample was then heated to 750 °C at 5 °C/min and held for 30 min before being cooled at the same rate. The program was repeated to eliminate the effects of impurities during the first program and the mass change from the second program was assumed to originate from the formation of oxygen vacancies. These relative changes in oxygen content were calibrated by TPR results. The precision of the microbalance was $\pm$1.0 μg, which leads to an accuracy of the oxygen nonstoichiometry $(3-\delta)$ to $\pm$0.0002. Reproducibility was demonstrated with four different batches of $La_{0.6}Sr_{0.4}Co_{0.2}Fe_{0.8}O_{3-\delta}$, which showed oxygen content $(3-\delta)$ at 700 °C within 0.001.

The TPR calibration was also checked by TGA and used similar experimental parameters unless noted otherwise. The flow balancing and blank experiments were performed in 30 mL/min of 5% H_2/N_2, in which 15 mL/min of N_2 and 10% H_2/N_2 was used as the carrier and auxiliary gas, respectively. The sample was heated to 600 °C at 5 °C/min and held for 30 min. The effluent was monitored by a MKS Instruments Cirrus mass spectrometer (MS). MS data were aligned with the TGA-DSC data by measuring the delay time between instruments and acquired in selected ion mode (SIM) using the electron multiplier detector.

2.5 Oxygen Vacancy Formation Under Inert Environments

Experiments were conducted on both a Thermo-Finnigan Trace Ultra differential scanning quadrupole (DSQ) gas chromatograph/mass spectrometer (GC/MS) and Autochem II 2920 instrument equipped with a TCD. For the GC/MS, samples were loaded in the same manner as for the TPR system. Data for the GC/MS were obtained using SIM and a 3 eV detector gain. For the Autochem, samples were loaded on top of quartz wool in fused quartz reactors. A TCD was used for easier quantification because the proper pretreatment led to only oxygen leaving the sample. The TCD signal was calibrated using the instrument's gas calibration feature. In both arrangements, samples (100 mg) were pretreated in 30 mL/min flow of an oxygen environment (20%O_2/He for GC/MS and 10%O_2/He for Autochem) at 850 °C (10 °C/min) with an isothermal hold for 20 min and then cooled under the same flows. Once near room temperature (less than 75 °C), the flow was switched to He at 30 mL/min and the tubing was purged for 1 h. Sample were heated to 900 °C at 10 °C/min and held there for 20 min.

3 Results and Discussion

3.1 Solid-state Reaction Monitored by In-situ TGA, XRD, and MS

To ensure the formation of the perovskite structure, the solid-state reaction was observed by in-situ techniques. As shown in Fig. 1, the synthesis reaction was monitored by TGA with the effluent being followed by MS. Results were in good agreement as the effluent spectra match well with mass changes. During milling, an interaction between water and the precursors developed. The interaction was denoted by the sharp mass loss and large evolution of water (m/z = 18) between 350 and 400 °C. Near 250–300 °C, a minor mass change and CO_2 (m/z = 44) detection was

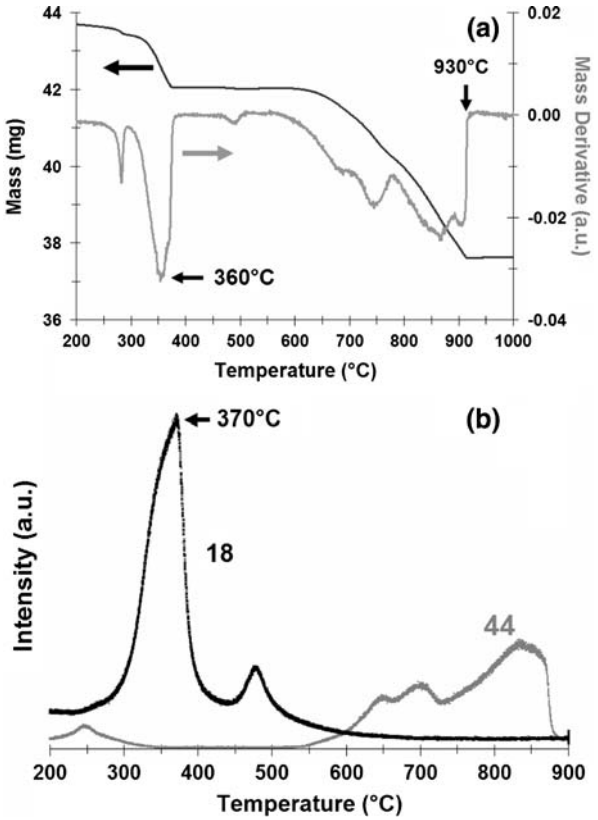

Fig. 1 Temperature-programmed solid-state reaction for $La_{0.6}Sr_{0.4}Co_{0.2}Fe_{0.8}O_{3-\delta}$ monitored by (**a**) TGA and (**b**) MS

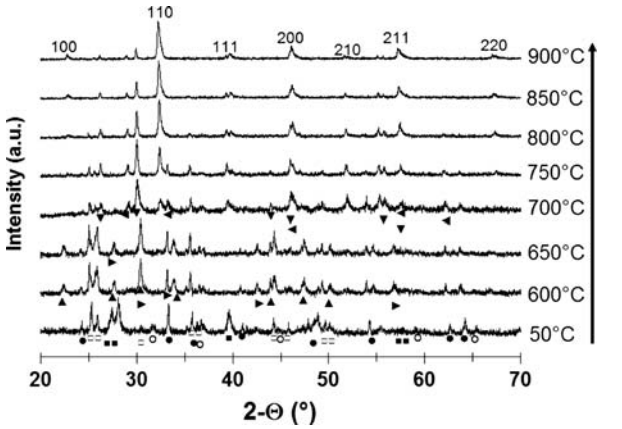

Fig. 2 Solid-state reaction for $La_{0.6}Sr_{0.4}Co_{0.2}Fe_{0.8}O_{3-\delta}$ monitored by XRD. Peak designations are as follows: Fe_2O_3 (●), $SrCO_3$ (□), La_2O_3 (■), Co_3O_4 (○), $LaSrFeO_4$ (►), $La_2O(CO_3)_2$ (▲), $LaSrCoO_4$ (▼), and SrO (◄). Numerical values indicate Miller indices for cubic perovskite phase

caused by CO_2 adsorbed from the atmosphere. More interestingly, the decomposition of $SrCO_3$ was not noticed until higher temperatures. Phase stability of the carbonate species will be discussed with aid from XRD. The carbonate species eluted over a broad range that begins near 550 °C and ends near 900 °C. In addition to CO_2 forming in this region, O_2 was also consumed from the air to bring the material closer to stoichiometric. The change in the mass derivative in near 800 °C indicates where this consumption likely occurred. It was in agreement with the temperature that perovskite phase forms during the XRD experiment discussed next. Due to the high temperature of this process and presumably slow kinetics (from the broad peak), a solid-state reaction temperature of 1,000 °C was selected.

Further insight into the carbonate species evolution and the perovskite phase formation was, as shown in Fig. 2, given by XRD. At 50 °C, a mixture of the precursors existed. By 700 °C, $SrCO_3$ was no longer present, but the carbonate species did not escape the sample. The carbonate groups combined with La to form $La_2O(CO_3)_2$, which was only present until 700 °C. The La carbonate compound ($La_2O(CO_3)_2$) that formed by 600 °C appeared to correspond to the mass loss and CO_2 formation near 700 °C. Free of the carbonate group, some of the Sr began to form mixed oxide compounds with Fe and Co. At 700 °C, the perovskite phase began to form. The remaining $SrCO_3$ decomposed to SrO, which then entered into the perovskite phase. The high temperature transition of $SrCO_3$ to SrO aligned well with mass loss and CO_2 formation near 900 °C. XRD results also indicated that a temperature higher than 900 °C was needed for a single phase material since remnants of the impurity species still exist at 900 °C. Since 1,000 °C was used, mass specific surface areas were near 1 m^2/g.

3.2 Bulk Structure Under Ambient Conditions

The bulk structure of the samples under ambient conditions was determined using XRD and TPR. As shown in Fig. 3 from XRD, unit cell parameters were calculated from 10 total batches with the error bars calculated from pooled deviations. The unit cell length decreased linearly as the Co content increased. The size effect was expected because Co ($r = 0.53$ Å for Co^{+4} in octahedral coordination) is generally smaller than Fe ($r = 0.585$ Å for Fe^{+4} in octahedral coordination) when the elements are in a similar chemical environment (oxidation state, coordination, spin state). If the addition of Co led to an increase in the formation of oxygen vacancies, the cations would reduce and cause an increase in the unit cell length (e.g., $r = 0.61$ Å for high-spin Co^{+3} in octahedral coordination). Related to a smaller unit cell, an increase in the unit cell symmetry, even though all samples have rhombohedral symmetry, occurred. The rhombohedral phase approaches the cubic phase as the angle approaches 60°, the value for cubic symmetry. The approach towards cubic symmetry was expected as the Co content increased. When Co content increased, the

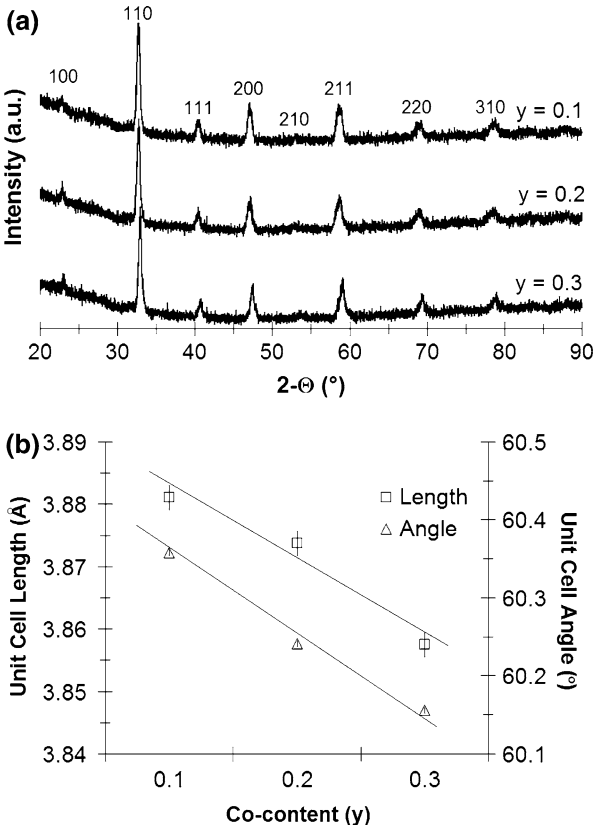

Fig. 3 Structural characterization for $La_{0.6}Sr_{0.4}Co_yFe_{1-y}O_{3-\delta}$. (**a**) XRD patterns. Values indicate Miller indices for cubic perovskite structure. (**b**) Calculated unit cell parameters

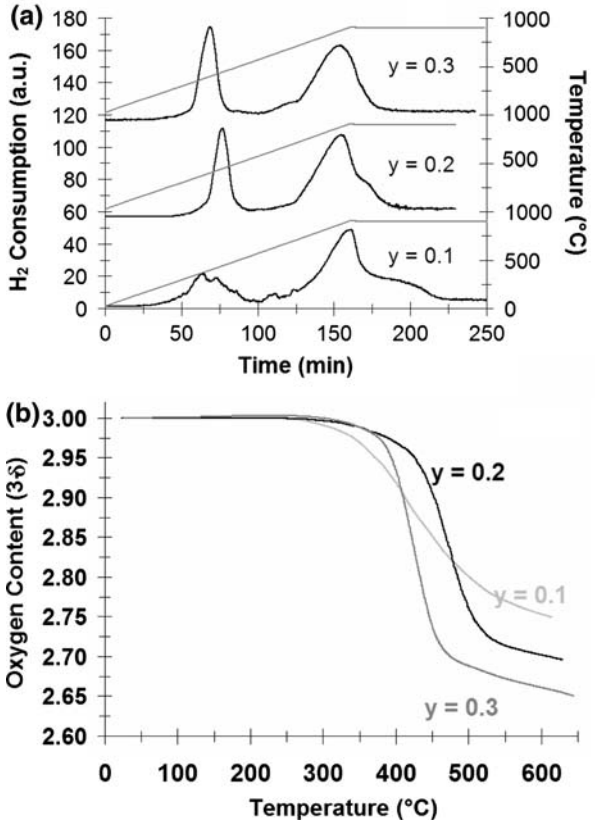

Fig. 4 TPR for $La_{0.6}Sr_{0.4}Co_yFe_{1-y}O_{3-\delta}$ in 10% H_2/N_2. (**a**) Raw data and (**b**) Degree of reduction calculated from (**a**)

tolerance factor approached unity (an indicator of increased symmetry [9]). A linear trend existed for the angle that is similar to unit cell length, which again suggested that the unit cell changes were solely caused by size difference between Co and Fe and not by oxidation state changes.

Based on the literature for other perovskite-type oxides containing La, Sr, Co, and Fe, the samples discussed in this study were expected to be stoichiometric under ambient conditions [5, 8]. Generally, samples containing more La than Sr were expected to be stoichiometric with respect to oxygen. XRD results discussed earlier in this study inferred that the materials do obey this generalization. However, a discrepancy existed in the literature for $La_{0.6}Sr_{0.4}Co_{0.2}Fe_{0.8}O_{3-\delta}$ about the oxygen content under ambient conditions [5, 7]. Thus, the oxygen content was measured by TPR as displayed in Fig. 4.

As will be discussed in more detail with in-situ XRD, the perovskite phase was stable through the low temperature reduction peak (300–600 °C). While the high temperature reduction peak (~900 °C) was associated with the reduction of the perovskite phase to its separate metal and metal oxide phases (although the initial part of this could be related to further formation of oxygen vacancies), the low temperature reduction was linked to the formation of oxygen vacancies. When the low temperature reduction feature was quantified, H_2 consumption increased linearly as Co content increased (0.251, 0.304, and 0.350 mole H_2 consumed per mole of sample for $y = 0.1$, 0.2 and 0.3, respectively). Assuming that the number of tetravalent sites in the starting material is determined by the A-site doping, these samples are expected to have 0.4 moles of tetravalent atoms (Co and Fe) per mole of sample. Then, the amount of H_2 consumed to reduce tetravalent ions to trivalent ones will be constant for each sample and will be equal to 0.2 moles per mole of sample. When this amount of H_2 is subtracted from the total H_2 consumption for each sample, the difference was equal to the amount of H_2 needed to reduce all of the Co from trivalent to divalent. Based on these observations, the initial assumption that the starting materials are stoichiometric at ambient conditions appeared valid and that Co ions reduced more readily than Fe (with all of Co being in divalent state at the end of the first reduction feature). This conclusion agreed with data for the samples studied with altered Sr content as long as the A-site has more La than Sr (e.g., $La_{0.8}Sr_{0.2}Co_{0.2}Fe_{0.8}O_{3-\delta}$) and was verified by isotopic exchange experiments, which will be presented in a

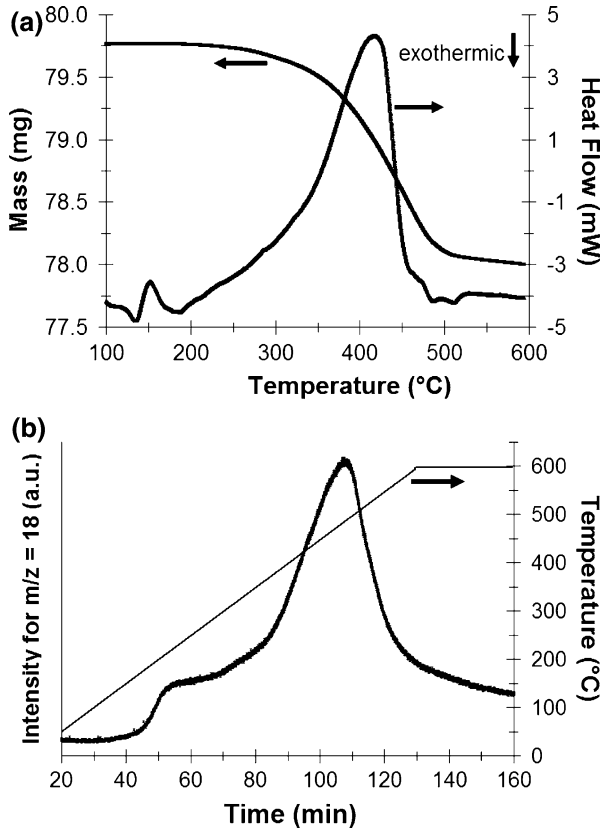

Fig. 5 In-situ TPR in TGA-DSC/MS in 10% H_2/N_2 for $La_{0.6}Sr_{0.4}Co_{0.2}Fe_{0.8}O_{3-\delta}$ (**a**) TGA-DSC signals (**b**) MS signals

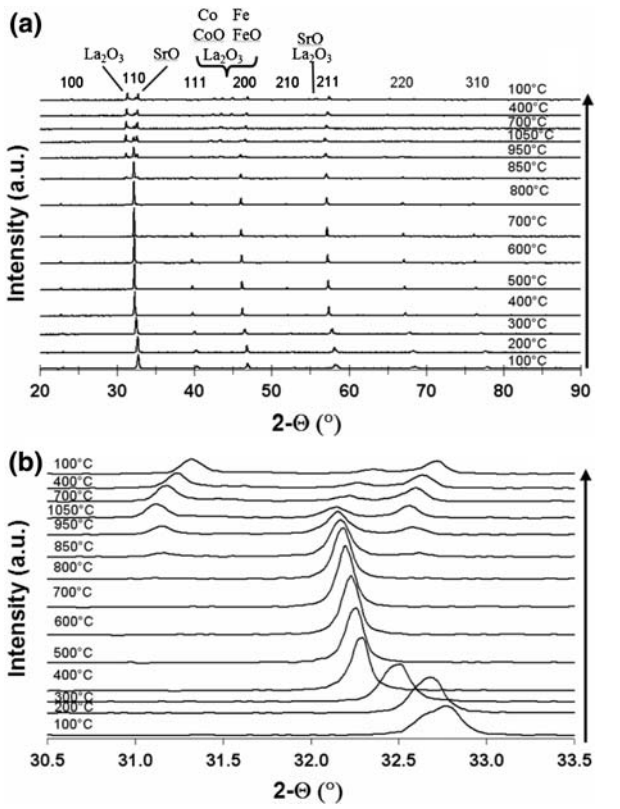

Fig. 6 In-situ TPR in XRD in 5% H_2/N_2 for $La_{0.6}Sr_{0.4}Co_{0.2}Fe_{0.8}O_{3-\delta}$ (**a**) overall results and (**b**) cubic (110) peak

future publication. Consequently, the degree of reduction or oxygen content as a function of temperature in a reducing medium was determined from the quantification of the TPR as is shown in Fig. 4b. The fact that Co reduced more easily than Fe suggested preferential electronic compensation, as reported for other formulations of Fe and Co based perovskite-type materials [5], following a slight reduction. However, evidence also indicates that preferential electronic compensation does not occur [18]. The trends in the degree of reduction will be discussed in Sect. 3.3.

The low temperature reduction feature was also examined for $La_{0.6}Sr_{0.4}Co_{0.2}Fe_{0.8}O_{3-\delta}$ using simultaneous TGA-DSC/MS (Fig. 5). In addition to providing further information about the formation of oxygen vacancies during the reduction, the TGA-DSC/MS experiment provided confirmation of the TCD quantification. For the simultaneous reduction experiment, good agreement was found between the MS and TGA-DSC signals. The mass change, water formation, and endothermic heat flow aligned at a similar temperature. The relatively small endothermic signal suggested that the reduction does not accompany a phase change. Moreover, the mass loss matched the prediction for this formulation from conventional TPR. The mass loss corresponded to 10% of the sample's oxygen content or a change from $ABO_{3.0}$ to $ABO_{2.7}$.

As alluded to earlier, the reduction was also followed by in-situ XRD and is shown in Fig. 6. The perovskite phase was solely present until 850 °C. At and above this temperature, the individual metal and metal oxide species formed as the perovskite phase was destroyed. By taking a closer look at the (110) cubic line, the loss of intensity at high temperatures coincided with the formation of new phases. The behavior of this line also revealed the source of H_2 consumption at low temperatures. Due to thermal effects, the line shifted to lower $2-\Theta$ values (larger d-spacing) through thermal expansion. Thermal expansion was expected to occur linearly with temperature as it did above 400 °C. However, the peak location abruptly moved to lower values between 200 and 400 °C. Additional chemical expansion occurred through the reduction of B-site cations that takes place simultaneously with the formation of oxygen vacancies. Upon cooling, the reversal of the thermal expansion occurred, but the peaks did not return to the initial values due to irreversible chemical expansion. More discussion is provided for these results in Sect. 3.3.

3.3 Effect of Temperature and Environment Upon the Bulk Structure

With the structure established for the samples under ambient conditions, the high temperature bulk structure was determined. In addition to temperature, the effect of environment was also studied. The environments used in the study are air, inert (He and N_2), and H_2 (5% or 10%/N_2). Oxygen content of the samples in air was determined by TGA and shown in Fig. 7. Oxygen content was in thermal equilibrium with the environment during the experiment because the mass held steady when the maximum temperature was reached and retraced itself upon cooling (data not shown). Oxygen vacancies formed most readily for the sample with low Co content. Moreover, the least amount of oxygen vacancies formed for the sample with intermediate Co content. As compared to the results in 10% H_2/N_2 in Fig. 4b, the amount of oxygen vacancies was much smaller in air. Therefore, the results in air can be compared to the initial reduction under the reducing environment. In both cases, the sample with the lowest Co content formed oxygen vacancies more easily initially.

The unit cell symmetry and size in air were determined as a function of temperature by in-situ XRD. As shown in Fig. 8, diffraction patterns for five cubic Miller indices that revealed the most pronounced changes upon the transition from rhombohedral to cubic symmetry are presented for $La_{0.6}Sr_{0.4}Co_{0.2}Fe_{0.8}O_{3-\delta}$. In each region, the peak at low temperatures was broad to signify the multiple peaks that existed for the rhombohedral phase. As the temperature increased, the broad peaks transformed to a single, sharp peak that indicated cubic symmetry. The transformation occurred continuously with temperature rather than abruptly over one temperature change. That is, the multiple peaks kept getting closer together (while moving to the left due to thermal expansion) as the temperature increased. The transformation was complete near 550 °C for

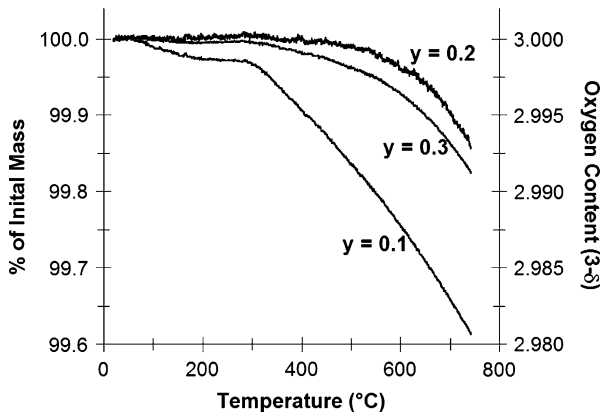

Fig. 7 Temperature-programmed oxygen vacancy formation in TGA-DSC for $La_{0.6}Sr_{0.4}Co_yFe_{1-y}O_{3-\delta}$ in air

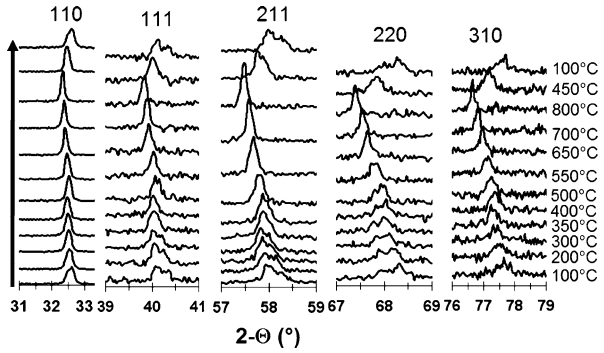

Fig. 8 Diffraction patterns for $La_{0.6}Sr_{0.4}Co_{0.2}Fe_{0.8}O_{3-\delta}$ as a function of temperature in air

$La_{0.6}Sr_{0.4}Co_{0.2}Fe_{0.8}O_{3-\delta}$. Changes were reversible with temperature as the peaks revert to multiple peaks upon cooling.

Unit cell parameters were calculated from the XRD patterns for the 3 samples as shown in Fig. 9. As the transition occurred, the rhombohedral unit cell angle approached 60°. Once it was complete, the angle remained at a value of 60°. The transition temperature decreased as the Co amount increased. The transition was not completed until 800 °C for the low Co amount while it was finished

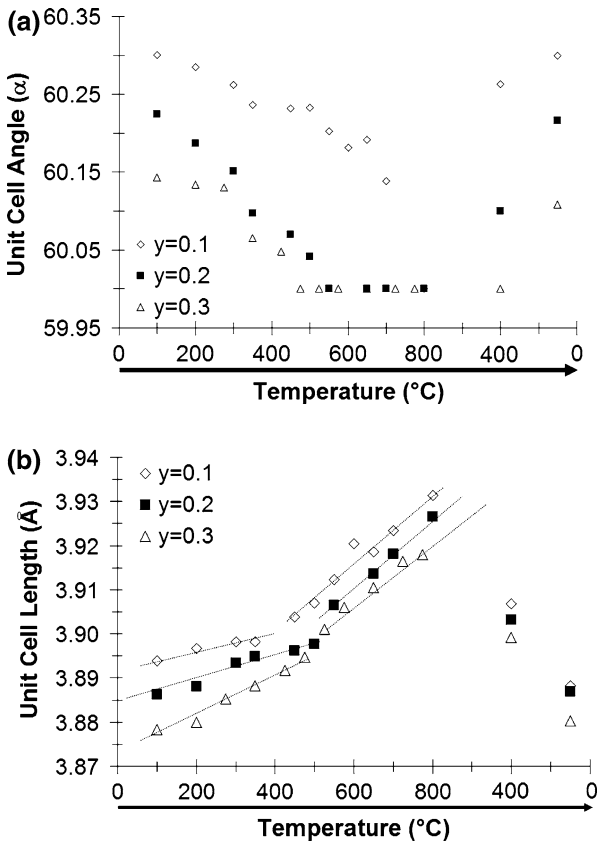

Fig. 9 Unit cell parameters (**a**) angle and (**b**) length for $La_{0.6}Sr_{0.4}Co_yFe_{1-y}O_{3-\delta}$ as a function of temperature in air

before 500 °C for the high Co amount. The differences are explained by the size and reducibility differences between Co and Fe as stated earlier. Additionally, the unit cell length was a strong function of temperature. Using the concept of linear thermal expansion, it was expected that the length would increase linearly with temperature. It is common for thermal expansion of these materials to be reported with a single value over a large temperature range (e.g., [19]). However, the results showed two distinct regions (indicated by the lines on Fig. 9b) of linear expansion. Although the phase transition may play a role, the regions appear to be separated by the temperature at which oxygen vacancies initially formed. Since the temperature at which the thermal expansion behavior changed appears to progress through a maximum with the Co content, the change is believed to be caused by the formation of oxygen vacancies and not by the transition to the cubic phase. For each region, TECs are presented in Table 1. The results are compared to TECs measured by the same technique for commercial samples of potential SOFC electrolytes. Due to chemical expansion (e.g., [20, 21]) in addition to thermal expansion, the lattice expanded more in the high temperature region compared to the low temperature region where only thermal expansion occurred. In the low temperature region, expansion increased with Co content while little dependence upon Co content was observed in the high temperature region. Some of the TEC values previously reported in the literature appear to be close to an average of the values measured in this work for the two regimes (e.g., 17.5 ppm/°C previously reported for $La_{0.6}Sr_{0.4}Co_{0.2}Fe_{0.8}O_{3-\delta}$ [19]).

High temperature structural properties were also monitored under inert environments. The experiments were first performed with a GC/MS so several ions could be followed. Once the pretreatment was optimized, only oxygen evolved from the samples and the results are shown in Fig. 10a. With only oxygen eluting from the sample, the experiments were repeated with a TCD to quantify the oxygen amount as shown in Fig. 10b. When comparing m/z = 32 from the GC/MS and the TCD signal, the signals matched well confirming that the TCD signal was solely from oxygen evolution. Compared to literature reports on oxygen evolution from perovskite-type materials [22, 23], the peaks shown in Fig. 10 were much more broad. The overlap of the peaks may be attributed to lower surface areas than in the literature [24]. Oxygen evolution peaks from perovskite-type oxides have been discussed in the literature and the findings will be briefly outlined. The low (termed α desorption) and high temperature evolution (termed β desorption) included oxygen from the bulk and were strong function of the material's composition [23]. The α-oxygen was linked to the reduction of tetravalent species while the β-oxygen was associated with the partial reduction of trivalent species and linked to the material's anionic mobility. Applying these findings to the present work, the β-oxygen peak was largest for the sample with the intermediate Co content and it would be expected to have the highest anionic mobility.

Additionally, the oxygen evolution, measured by the TCD, was quantified as shown in Fig. 10c. The total oxygen eluting from the samples was much greater than in air, but less than under reducing conditions. Results again showed that the sample with the intermediate Co amount is initially the least reducible. From the raw signal, it was expected since it has much smaller α desorption than the other samples. However, this sample contained the largest high temperature oxygen evolution peak. The values shown for $La_{0.6}Sr_{0.4}Co_{0.2}Fe_{0.8}O_{3-\delta}$ in Figs. 4b and 10c agreed with data available in the literature under similar conditions [5, 25].

Diffraction patterns as a function of temperature under inert conditions (N_2) are shown in Fig. 11. As discussed earlier, peaks shifted to lower $2-\Theta$ values due to thermal and chemical expansion. Merging of the lines demonstrated that the rhombohedral to cubic transition occurred near 500 °C.

Unit cell parameters for $La_{0.6}Sr_{0.4}Co_{0.2}Fe_{0.8}O_{3-\delta}$ determined as a function of environment are shown in Fig. 12. As indicated by the rhombohedral angle reaching 60°, the transition from rhombohedral to cubic symmetry was completed by 500 °C under reducing conditions. The phase transition occurred at a similar temperature under all environments which indicated that the additional chemical expansion did not force the transition to a higher temperature. Rather, it indicated that the thermal behavior of the A-site cations occurred more rapidly with temperature than expansion of the B-site cations. The effects of

Table 1 TEC (ppm/°C) determined by change in lattice parameters as a function of temperature for $La_{0.6}Sr_{0.4}Co_yFe_{1-y}O_{3-\delta}$ and selected SOFC electrolytes

Sample	TEC (ppm/°C)	Temperature range (°C)
y = 0.1	5	100–350
	20	450–800
y = 0.2	8	100–500
	22	550–800
y = 0.2 (N_2)	12	100–400
	23	500–1,000
y = 0.2 (5% H_2/N_2)	38	100–400
	12	500–1,000
y = 0.3	12	100–475
	18	525–800
Ceria (GCD)	13	100–1,000
Zirconia (YSZ)	11	100–1,000

Experiments performed under air unless otherwise noted

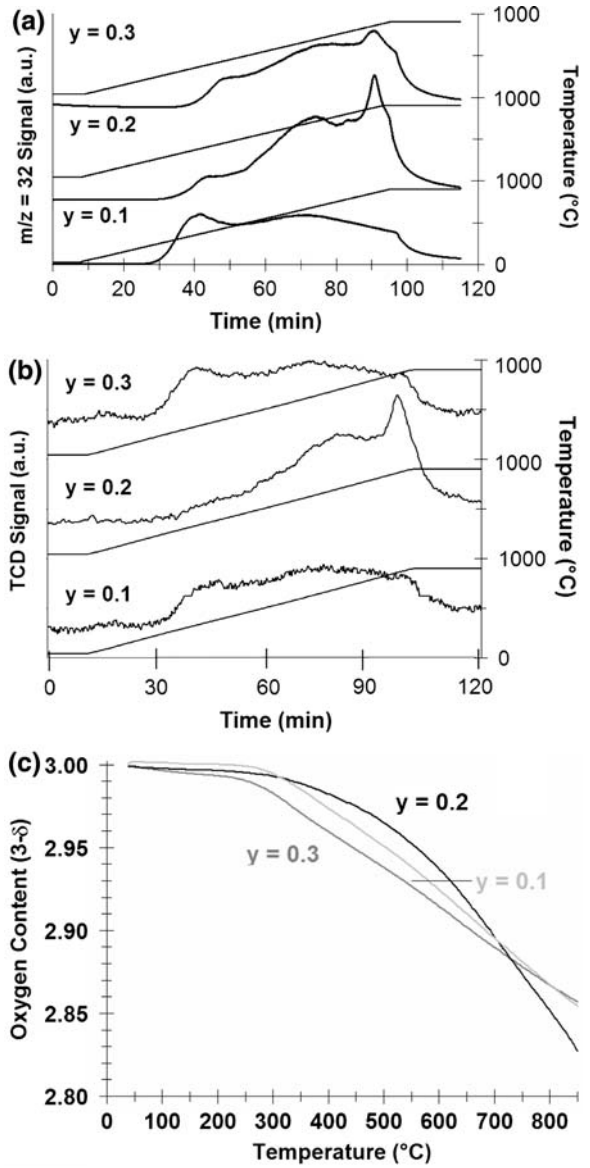

Fig. 10 Oxygen evolution measured in inert environments (He) by (**a**) GC/MS, (**b**) TCD, and (**c**) quantified using TCD for $La_{0.6}Sr_{0.4}Co_yFe_{1-y}O_{3-\delta}$

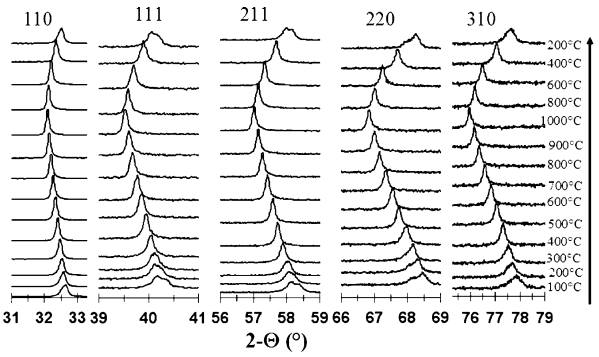

Fig. 11 Diffraction patterns for $La_{0.6}Sr_{0.4}Co_{0.2}Fe_{0.8}O_{3-\delta}$ as a function of temperature in nitrogen

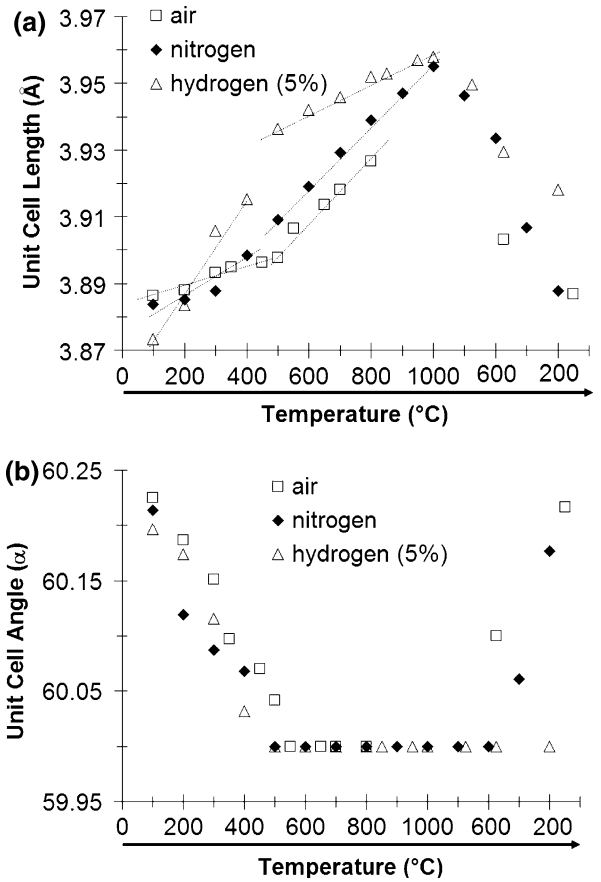

Fig. 12 Unit cell parameters (**a**) length and (**b**) angle for $La_{0.6}Sr_{0.4}Co_{0.2}Fe_{0.8}O_{3-\delta}$ as a function of temperature and environment

the thermal expansion are much more dominant and the chemical expansion has very little influence over the transition temperature. As the B-site cations reduce, it becomes larger which would lead to a smaller tolerance factor. A smaller tolerance factor leads to a less symmetric unit cell. However the chemical expansion did not appear to influence the transition temperature suggesting that the thermal expansion of the ions was more important.

As seen in Fig. 12, the variation of the unit cell length with temperature can again be split into 2 regimes based upon the slope change. TECs for each regime are presented as a function of atmosphere in Table 1. In the low temperature region, the slope increased as the reducing nature of the environment increased. The trend in the low temperature slope occurred because additional chemical expansion was observed at lower temperatures under more reducing conditions. Reducing conditions led to a much lower TEC compared to less reducing environments in the high temperature region because of the greater extent to which chemical expansion occurred in the first region.

4 Conclusions

$La_{0.6}Sr_{0.4}FeO_3$ based perovskite-type oxides were confirmed to need high synthesis temperatures for high purity preparation via solid-state techniques and to be stoichiometric with respect to oxygen under ambient conditions. Ambient stoichiometry, generally assumed but not proven, is confirmed by the lack of hysteresis during heating and cooling as observed by TGA-DSC for rates up to 5 °C/min. The discrepancy reported [5, 7] upon the ambient stoichiometry of $La_{0.6}Sr_{0.4}Co_{0.2}Fe_{0.8}O_{3-\delta}$ may be caused by differences in cooling rates (not always given) following treatments prior to analyses. Hysteresis likely arises in air at high heating and cooling rates.

With the ambient structure confirmed, high temperature structural features were monitored as a function of environment and Co content in the Fe-rich regime. For deep reductions (i.e., under H_2), the degree of reduction was proportional to Co content. These results support that preferential oxidation of Fe over Co (an idea recently debated [6, 18]) occurred. Under milder conditions, a non-linear dependency existed for the formation of oxygen vacancies with respect to Co content. This non-linearity was not in agreement with increasing oxygen vacancy formation with increasing Co content as commonly reported for other formulations [5, 6, 8, 25]. Since it existed under equilibrium (under air) and non-equilibrium (under inert atmosphere and also note that the peak reduction temperature under H_2 follows the same trend) conditions, the behavior must be caused by a phenomenon that influence both thermodynamic and kinetic parameters. The trends may be attributed to an electronic structure transition in which electrons go from being described as localized for Co-rich samples to delocalized for Fe-rich samples [1]. Possibly in agreement with interesting behavior reported for $LaCo_{0.9}Fe_{0.1}O_{3-\delta}$ [26] the non-linearity could also be related to the low Co content in $La_{0.6}Sr_{0.4}Co_{0.1}Fe_{0.9}O_{3-\delta}$ that induces different behavior. The effects of this behavior upon the surface properties of these materials is also addressed [27].

Finally, the rhombohedral to cubic transition occurred at lower temperatures as Co content increased. The transition showed much less dependence upon environment than temperature and Co content. The transition may influence the high temperature bulk and surface properties of these materials. A change in thermal expansion behavior was likely caused by the simultaneous chemical expansion related to the formation of oxygen vacancies. Since it appeared to be independent of the rhombohedral to cubic phase transition, inferred phase transitions reported in the literature from non-linear dilatometry results may be inaccurate and should be viewed with caution. Moreover, dilatometry did not detect the transition to the cubic phase. The phase transition and change in thermal expansion behavior are likely important towards high temperature properties and in consideration of thermal compatibility with SOFC electrolytes. Treatment of thermal expansion over a large temperature range leads to an underestimate of the TEC appropriate for high temperature applications.

Acknowledgments The financial support provided for this work by the Ohio Coal Development Office and the Ohio Department of Development through a Wright Center of Innovation is gratefully acknowledged. The authors also thank Rick B. Watson for technical assistance in the initial stages of this research.

References

1. Adler SB (2004) Chem Rev 104:4791
2. Mizusaki J, Yoshihiro M, Yamauchi S, Fueki K (1985) J Solid State Chem 58:257
3. Mizusaki J, Mima Y, Yamauchi S, Fueki K, Tagawa H (1989) J Solid State Chem 80:102
4. Mizusaki J, Moir N, Takai H, Yonemura Y, Minamiue H, Tagawa H, Dokiya M, Inaba H, Naraya K, Sasamoto T, Hashimoto T (2000) Solid State Ionics 129:163
5. Stevenson JW, Armstrong TR, Carneim RD, Pederson LR, Weber WJ (1996) J Electrochem Soc 143:2722
6. Tai LW, Nasrallah MM, Anderson HU, Sparlin DM, Sehlin SR (1995) Solid State Ionics 76:259
7. Tai LW, Nasrallah MM, Anderson HU, Sparlin DM, Sehlin SR (1995) Solid State Ionics 76:273
8. Lankhorst MHR, ten Elshof JE (1997) J Solid State Chem 130:302
9. Pena MA, Fierro JLG (2001) Chem Rev 101:1981
10. Wang S, Katsuki M, Dokiya M, Hashimoto T (2003) Solid State Ionics 159:71
11. Petrov AN, Kononchuk OF, Andreev AV, Cerepanov VA, Kofstad P (1995) Solid State Ionics 80:189
12. Wiik K, Aasland S, Hansen HL, Tangen IL, Ødegard R (2002) Solid State Ionics 152–153:675
13. Qui L, Lee TH, Liu LM, Yang YL, Jacobson AJ (1995) Solid State Ionics 76:321
14. Kruidhof H, Bouwmeester HJM, van Doorn RHE, Burggraaf AJ (1993) Solid State Ionics 63–65:816
15. McIntosh S, Vente JF, Haije WG, Blank DHA, Bouwmeester HJM (2006) Solid State Ionics 177:1737
16. Vente JF, McIntosh S, Haije WG, Bouwmeester HJM (2006) J Electrochem Soc 10:581
17. Yang ZH, Lin YS (2005) Solid State Ionics 176:89
18. Nemeth Z, Homonnay Z, Arva F, Klencsar Z, Kuzmann E, Hakl J, Vad K, Meszaros S, Kellner K, Gritzner G, Vertes A (2007) J Radioanal Nucl Chem 271:11
19. Petric A, Huang P, Tietz F (2000) Solid State Ionics 135:719
20. Adler SB (2001) J Am Ceram Soc 84:2117
21. Chen X, Yu J, Adler SB (2005) Chem Mater 17:4537
22. Yamazoe N, Teraoka Y, Seiyama T (1981) Chem Lett 1767
23. Seiyama T, Yamazoe N, Eguchi K (1985) Ind Eng Chem Prod Res Dev 24:19
24. Kaliaguine S, Van Neste A, Szabo V, Gallot JE, Bassir M, Muzychuk R (2001) Appl Catal A: Gen 209:345
25. Mantzavinos D, Hartley A, Metcalfe IS, Sahibzada M (2000) Solid State Ionics 134:103
26. Merino NA, Barbero BP, Ruiz P, Cadus LE (2006) J Catal 240:245
27. Kuhn JN, Ozkan US (2007) J Catal (accepted)